# Zonal flow suppression of microturbulent transport in the optimized stellarators W7-X and QSTK

Abhishek Tiwari[1,*], Joydeep Das[1], Jaya Kumar Alageshan[1], Gareth Roberg-Clark[2], Gabriel Plunk[2], Pavlos Xanthopoulos[2], Sarveshwar Sharma[3,4], Zhihong Lin[5] , Animesh Kuley[1,*]

[1]*Department of Physics, Indian Institute of Science, Bangalore 560012, India*
[2]*Max-Planck-Institut für Plasmaphysik, D-17491 Greifswald, Germany*
[3]*Institute for Plasma Research, Bhat, Gandhinagar 382428, India*
[4]*Homi Bhabha National Institute, Anushaktinagar, Mumbai, Maharashtra 400094, India*
[5]*Department of Physics and Astronomy, University of California Irvine, CA 92697, USA*
*Email: abhishektiwa@iisc.ac.in, akuley@iisc.ac.in*

### Abstract

We present a comparative study of turbulence transport in two optimized stellarator configurations: Wendelstein 7-X (W7-X) and a recent design called Quasi-Symmetric Turbulence Konzept (QSTK). Using global gyrokinetic simulations with the Gyrokinetic Toroidal Code (GTC), we explore the role of zonal flows (ZFs) in suppressing electrostatic Ion Temperature Gradient (ITG) driven turbulence in both configurations. The simulations reveal that ZFs significantly reduce ion heat transport in both W7-X and QSTK, with a more pronounced impact on the latter configuration, as suggested by the apparently higher linear threshold ("critical") gradients for ITG modes. The study also highlights that, while both stellarators exhibit similar mode structures, the reduced ITG growth rates in QSTK contribute to the better performance regarding turbulence suppression, particularly at larger temperature gradients. The results support the notion that linear stability measures, in combination with nonlinear stabilization by zonal flows, can play an important role in the suppression of nonlinear heat fluxes.

*Keywords:* Simulations, Gyrokinetic, Microturbulence, Stellarator

## 1 Introduction

Recent advancements in stellarator [1] design and technology have significantly improved their plasma confinement capabilities, rendering them an increasingly promising approach in fusion research alongside the well-established tokamak designs. The stellarator has advantages over the tokamak, for instance, the absence of toroidal current, steady state operation, and lower magnetohydrodynamic (MHD) activity. However, these advantages come at the cost of breaking toroidal symmetry, which can lead to an increase in collisional transport, coupling of macro- and micro-instabilities, and stronger damping of zonal flows [2,3]. Design and optimization [4] of stellarators have led to better plasma confinement in cases like W7-X [5], which have achieved a performance closer to tokamaks. W7-X is an optimized stellarator that became operational in 2016. It has been confirmed that neoclassical transport in W7-X is reduced with respect to non-optimized stellarators [4,6]. However, turbulence has played a dominant role in limiting plasma performance in W7-X for specific heating scenarios. [7].

A primary obstacle in plasma confinement is the presence of micro-instabilities driven by the ion temperature gradient (ITG) and the trapped electron mode (TEM). Turbulence associated with these drift wave instabilities can lead to loss of plasma confinement by transporting energy and particles. In modern stellarator experiments such as W7-X, advanced diagnostic techniques like phase contrast imaging (PCI) are employed to measure and characterize ITG and TEM behaviour [8]. It has been found that the stability of the ITG mode depends upon the gradient ratio $\eta_i = L_{n_i}/L_{T_i}$ where $L_m = d\ln T_m/dr$ is the gradient length scale. The critical gradient (CG) is the threshold gradient for the onset of the ITG mode. One way to combat losses from ITG is to increase the size and heating power of the stellarator [9]. Another way is to address ITG itself by changing the plasma profiles [10]. Also, radio frequency waves are used to stabilize these micro-instabilities in fusion plasmas [11,12].

In addition to these strategies, shaping the magnetic field can further reduce losses due to micro-turbulence in the plasma core. Certain implementations of this strategy target the critical gradient of the mode [9], (CG-approach), producing the HSK stellarator, which exhibits the most significant critical gradient at half radius of all known stellarators. It has also been shown in Ref. [9] that this strategy can target the CG of the toroidal branch of the ITG mode without compromising MHD stability. Such optimization produces a quasi-helical symmetric configuration (QSTK) with strongly reduced ITG turbulence and acceptable levels of neoclassical losses, alpha particle confinement, and MHD stability, leading to improved ion confinement.

The Quasi-Symmetric Turbulence Konzept (QSTK) configuration has $N_{fp} = 6$, an aspect ratio of 7.5, neoclassical transport coefficient $\epsilon_{\text{eff}} < 1\%$ up to half radius, large rotational transform $> 1.6$ and $\simeq 5\%$ alpha particle losses for particles initialized at half radius. QSTK also features good MHD stability, small bootstrap current, and it admits coils of moderate complexity. In addition, flux-tube based gyrokinetic simulations suggest that the heat flux is significantly reduced compared to W7-X [9].

Several gyrokinetic simulations of micro-turbulence in stellarators have been done previously. For example, the global code EUTERPE [13] was used to study the effects of radial electric field on linear ITG instability in W7-X and LHD [14]. The effect of density gradient and micro-instabilities on turbulent heat transport in stellarators was performed with flux-tube code stella [15]. The electromagnetic gyrokinetic Vlasov flux-tube code GKV was used to study the impact of isotope ion mass on TEM driven turbulence and zonal flow in LHD stellarators [16]. The GENE flux-tube simulation has been used to study the effect of ZF dynamics and turbulent transport in stellarator geometry [17]. The codes GENE-3D, KNOSOS, and TANGO were used to compute the plasma profiles due to the combined effect of neoclassical transport, turbulent transport, and external particles in W7-X, QSTK and HSK stellarators [18, 19]. The GT5D code performed full-f global simulations in LHD and the collisionless zonal flow damping [20]. Global XGC-S [21] and GENE-3D [22] were used to carry out micro-turbulence simulations using adiabatic electrons in W7-X and LHD. The global gyrokinetic toroidal code GTC was used to perform the nonlinear global gyrokinetic simulations of micro-turbulence in LHD and W7-X, including the kinetic effect of electrons in stellarators [2, 23, 24]. In addition to these efforts, global fluid simulation of plasma turbulence in stellarators has been carried out using the GBS [25] and BSTING [26, 27] codes.

In previous works [2, 23, 24], the global gyrokinetic toroidal code GTC has been used to perform nonlinear global gyrokinetic simulations of micro-turbulence in LHD and W7-X, including the benchmark of ITG simulations with EUTERPE [28], the suppression of ITG by neoclassical ambipolar electric field and its effects on microturbulence in W7-X stellarator [29], the isotope effects [30], and the kinetic effect of electrons in stellarators. In this paper, we compare the effect of zonal flow on the turbulent transport driven by ITG turbulence with adiabatic electrons for the stellarators W7-X and QSTK. The paper is organized as follows: First, in Sec. 2, we briefly present the physics model and the numerical code employed. Then, in Sec. 3, we study the linear simulation of ITG in both stellarators. In Sec. 4, we perform the nonlinear simulations and evaluate the effect of zonal flow on the ITG turbulence. We conclude with some discussion in Sec. 5.

## 2    Simulation Model

In this paper, we use the global nonlinear code GTC [31] to perform collisionless gyrokinetic simulations of micro-turbulence. GTC has been extensively applied to simulate neoclassical and turbulent transport [24,32–34], Alfvén waves [35], energetic particles [36,37], and radio frequency waves [38–40] in toroidally confined plasmas. It has also been used to simulate the effect of collisional damping on zonal flow and their impact on transport [41].

GTC interfaces with VMEC [42], an ideal MHD code, to obtain the non-axisymmetric equilibrium of QSTK and W7-X, considering closed magnetic surfaces. This equilibrium data contains information on poloidal current, toroidal current, and magnetic field described as Fourier series in poloidal and toroidal direction, given by,

$$\mathcal{F}(\psi, \theta, \zeta) = \sum_n \left[ \mathcal{F}_c(\psi, \theta, n) \, \cos(n\zeta) + \mathcal{F}_s(\psi, \theta, n) \, \sin(n\zeta) \, \right]$$

where $(\psi, \theta, \zeta)$ are the poloidal flux, poloidal angle and toroidal angle, respectively. Here, n is
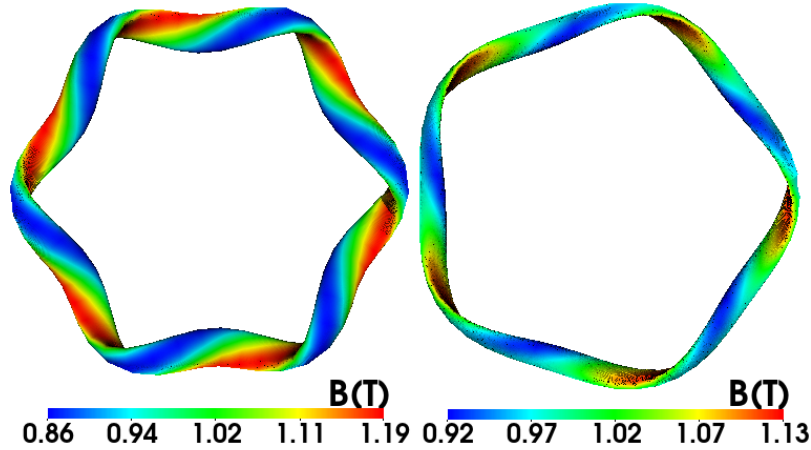
**Figure 1:** The magnetic field of the two stellarators: (Left) QSTK; (Right) W7-X on the flux surface with $\psi/\psi_w = 0.57$ ; the colors represent the corresponding strength of the magnetic fields.

the toroidal harmonic number and $\mathcal{F}_c$ and $\mathcal{F}_s$ are the Fourier coefficients specified on rectangular equilibrium mesh on the $\zeta = const.$ poloidal plane. GTC uses a global field-aligned mesh in real-space coordinates, which is used to represent all turbulence quantities. This provides computational efficiency without imposing any geometrical approximations. Further, this turbulence mesh only needs a small number of grid points in the parallel directions to resolve the drift-wave eigenmode structure due to the anisotropic nature of micro-turbulence. We note that the QSTK has 6 field periods ($N_{fp} = 6$), while the W7-X stellarator has 5 field periods ($N_{fp} = 5$). We exploit the $2\pi/N_{fp}$ periodicity, to simulate one period of each configuration, instead of the full torus.

In the present work, we assume that the electrons follow a Boltzmann distribution. The collisionless gyrokinetic Vlasov equation, which describes the thermal ions in an inhomogeneous magnetic field, is given by [23, 24]

$$\frac{d}{dt}f(\mathbf{X}, \mu, v_{||}, t) = \left[\frac{\partial}{\partial t} + \dot{\mathbf{X}} \cdot \nabla + \dot{v}_{||}\frac{\partial}{\partial v_{||}}\right] f = 0; \qquad \dot{\mathbf{X}} = v_{||}\boldsymbol{b} + \mathbf{v_d} + \mathbf{v_E} \tag{1}$$

$$\text{where,} \qquad \dot{v}_{||} = -\frac{1}{m}\frac{\boldsymbol{B^*}}{B} \cdot (\mu\nabla B + Z_i\nabla\phi)$$

$$\mathbf{v_d} = \frac{v_{||}^2}{\Omega}(\nabla \times \boldsymbol{b}) + \frac{\mu}{m\Omega}(\boldsymbol{b} \times \nabla B)$$

$$\mathbf{v_E} = \frac{c}{B}(\boldsymbol{b} \times \nabla\phi)$$

where $f(\mathbf{X}, \mu, v_{||}, t)$ is the particle distribution function, with $\mathbf{X}$ is the gyrocenter position, $\mu$ is the magnetic moment, $v_{||}$ is the parallel velocity, $Z_i$ is the ion charge, $m$ is ion mass, and $\phi$ is the electrostatic perturbed potential. $\boldsymbol{B}$ is the equilibrium magnetic field at the particle position, $\boldsymbol{B^*} = \boldsymbol{B} + \frac{Bv_{||}}{\Omega}\nabla \times \boldsymbol{b}$, and $\boldsymbol{b} = \frac{\boldsymbol{B}}{B}$. In the present work, we retain the zonal flow generated by the ITG turbulence, while neglecting the equilibrium radial electric field.

To reduce the particle noise in the simulation, GTC uses the $\delta f$ method [43]. In this scheme, we decompose the distribution function into an unperturbed equilibrium part and a perturbed part as $f = f_0 + \delta f$. Further, the propagator in Eq.(1) can be separated into an equilibrium part $L_0$ and a perturbed part, $\delta L$ so that the Eq.(1) can be written as $(L_0 + \delta L)(f_0 + \delta f) = 0$, where

$$L_0 = \frac{\partial}{\partial t} + (v_{||}\mathbf{b} + \mathbf{v_d}) \cdot \nabla - \frac{1}{m}\frac{\boldsymbol{B^*}}{B} \cdot (\mu\nabla B)\frac{\partial}{\partial v_{||}},$$

$$\delta L = \mathbf{v_E} \cdot \nabla - \frac{1}{m}\frac{\boldsymbol{B^*}}{B} \cdot Z_i\nabla\phi\frac{\partial}{\partial v_{||}}$$

The equilibrium distribution function $f_0$ is determined by the condition $L_0 f_0 = 0$. The solution of this equation is approximated to be the local Maxwellian

$$f_0 = \frac{n_i}{(2\pi T_i/m)^{3/2}} \exp\left(-\frac{2\mu B + mv_{||}^2}{2T_i}\right)$$

where $n_i$ and $T_i$ are the equilibrium ion density and temperature, respectively. Next, we define the particle weight $w = \delta f/f_0$, and the evolution of this dynamical variable corresponding to thermal ions is given by

$$\frac{dw}{dt} = (1-w)\left[-\mathbf{v_E}\cdot\frac{\nabla f_0}{f_0} + \frac{Z_i}{m f_0}\frac{\boldsymbol{B^*}}{B}\cdot\nabla\phi\frac{\partial f_0}{\partial v_{||}}\right] \tag{2}$$

We note from Eq.(2) that we have neglected the neoclassical effect, since the term $\mathbf{v_d}\cdot\nabla f_0$ does not appear in the above equation. The electrostatic potential $\phi$ is obtained from the following gyrokinetic Poisson equation [33, 34],

$$\phi - \tilde{\phi} = \frac{T_i}{n_i Z_i^2}(Z_i \bar{n}_i - e n_e), \tag{3}$$

where $\tilde{\phi}$ is the second gyro averaged potential, $\bar{n}_i$ and $n_e$ are the ion and electron guiding center density, respectively. In GTC, we can decompose the electrostatic potential $\phi$ and ion density perturbation $\bar{n}_i$ into zonal and non-zonal components as

$$\phi = \langle\phi\rangle + \delta\phi,$$
$$\bar{n}_i = \langle\bar{n}_i\rangle + \delta\bar{n}_i,$$

with $\langle\delta\phi\rangle = 0$, $\langle\delta\bar{n}_i\rangle = 0$, $\langle\delta n_e\rangle = 0$ and the $\langle\cdots\rangle$ represent flux-surface averaging. The non-zonal part of gyrokinetic Poisson equation thus becomes

$$\delta\phi - \delta\tilde{\phi} = \tfrac{T_i}{n_i Z_i^2}(Z_i\,\delta\bar{n}_i - e\,\delta n_e)\ ; \tag{4}$$

$$\delta\tilde{\phi} = \tfrac{1}{2\pi}\int d^3\mathbf{v}\ \int d^3\mathbf{X}\ f_0(\mathbf{X})\ \delta\bar{\phi}(\mathbf{X})\ \delta(\mathbf{X} + \rho - \mathbf{x}) \tag{5}$$

where $\delta n_e = n_{0e}\delta\phi/T_e$, $T_e$ is the electron temperature. $\mathbf{x}$ and $\mathbf{X}$ are the particle position and the particle guiding center position coordinates, respectively, and $\rho$ is the gyro-radius vector. $\delta\bar{\phi}$ is the first gyro-averaged perturbed potential given by

$$\delta\bar{\phi}(\mathbf{X}) = \int d^3\mathbf{x}\int\frac{d\alpha}{2\pi}\ \delta\phi(\mathbf{x})\ \delta(\mathbf{x} - \mathbf{X} - \rho),$$

where $\alpha$ denotes the gyro-phase. Similarly, the ion perturbed density at the location of the guiding center is given by

$$\delta\bar{n}_i(\mathbf{x}) = \int d^3\mathbf{X}\int\frac{d\alpha}{2\pi}\ \delta f(\mathbf{X})\ \delta(\mathbf{x} - \mathbf{X} - \rho).$$

A finite difference method is used to obtain the non-zonal electrostatic potential, while the flux-surface average gyrokinetic equation for the zonal component of electrostatic potential is computed using traditional integration in GTC.

## 3   Linear Simulation of ITG in stellarators

### 3.1   ITG instability in W7-X

We apply the same plasma profiles for both QSTK and W7-X to simulate the linear and nonlinear physics of ITG turbulence in the two optimized stellarators and the effect of zonal flow. In Fig. (2) and Fig. (3) we show the temperature profile and safety factor, respectively, for W7-X and QSTK. The ion density $n_i$, electron density $n_e$, and electron temperature $T_e$ are assumed to be constant along radius, i.e., $\eta_i = \infty$. The definition of radial coordinate is $r = a\sqrt{\psi/\psi_w}$, with $a$ the minor
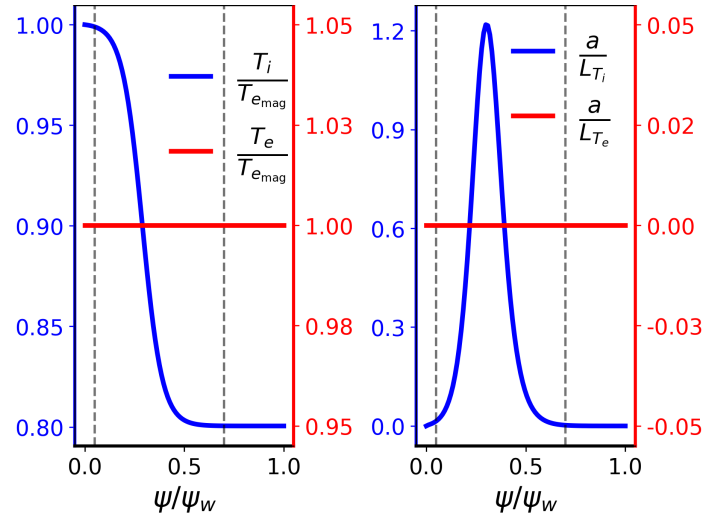
**Figure 2:** (Left) Radial profiles of equilibrium ion (blue) and electron (red) temperatures. Both quantities are normalized by $T_{e_{mag}}$, the electron temperature on-axis. (Right) We plot the quantity $a/L_{T_m}$ {m={**i**ons,**e**lectrons}} as defined in Eq. (6). The dashed vertical lines indicate the simulation domain.
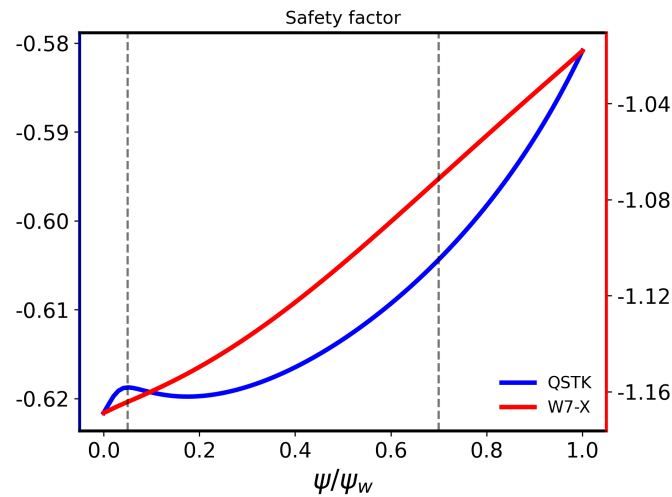
**Figure 3:** Safety factor (q) for both W7-X (red) and QSTK (blue) are shown in continuous curve and the dashed lines indicate the simulation domain.
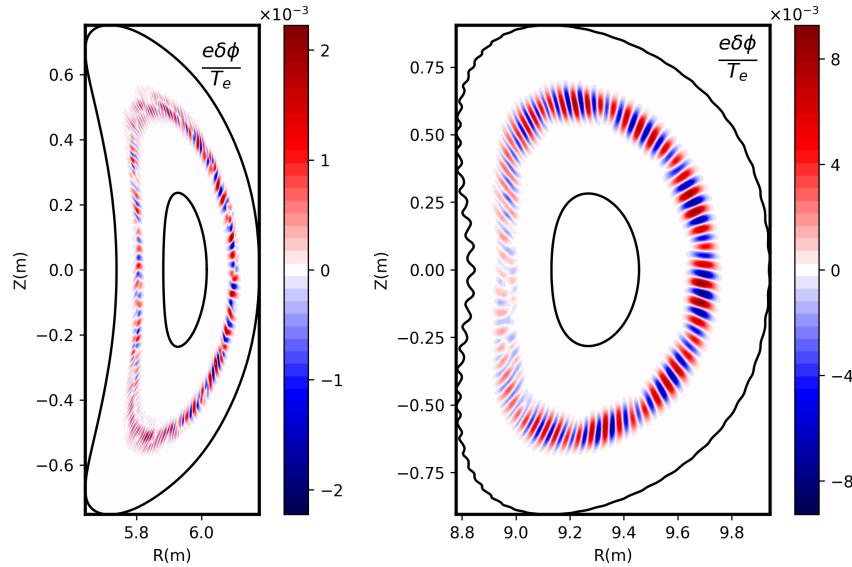
**Figure 4:** The normalized electrostatic perturbed potential, $e\delta\phi/T_e$, on the $\zeta = 0$ poloidal plane in the linear phase, at $t = 25.0R_0/C_s$ for W7-X (left) and at $t = 37.5R_0/C_s$ for QSTK (right) with the ion temperature gradient $a/L_{T_i} = 1.21$. The black curves represent the inner and outer simulation boundaries. We choose the simulation domain upto $\psi_{outer} = 0.7\psi_w$ since there is a numerical issue with the EFIT data in QSTK. Also, we choose the plasma profile in a manner so that the mode does not spreads to the boundary of domain.

radius corresponding to $\psi_w$. The temperature gradient length scale, measured relative to the minor radius $a$, is defined as

$$\left(\frac{a}{L_{T_m}}\right) = -2\frac{\partial \ln T_m}{\partial \tilde{\psi}}\sqrt{\tilde{\psi}}, \quad \text{where} \quad \frac{1}{L_{T_m}} = -\frac{\partial \ln T_m}{\partial r} \tag{6}$$

Here, $\tilde{\psi} = \psi/\psi_w$, with $m = \{i, e\}$ and $\psi_w$ represents the flux at the last close flux surface. The boundaries of the radial simulation domain are $\psi_{inner} = 0.05\psi_w$ and $\psi_{outer} = 0.7\psi_w$. The maximum value of the ion temperature gradient length scale measured relative to minor radius is 1.21 as shown in Fig. 2. Other parameters used in the simulation are major radius $R_0 = 5.58$m, magnetic field on axis $B_0 = 2.79$T and electron temperature $T_e = 6.50$ keV. After the convergence test, we use 9 parallel grid points, 121 radial grid points, 4400 poloidal grid points, 200 ions per cell, and $\Delta t = 0.01R_0/C_s$ where $C_s/R_0 = 14.11 \times 10^4 \text{sec}^{-1}$ and $C_s = \sqrt{T_e/m_i}$ is the ion acoustic speed. Fig. 4 (left) represents the electrostatic potential of ITG mode on $\zeta = 0$ poloidal plane during the linear phase of the nonlinear simulation at $t = 25.0R_0/C_s$. The mode is localized at the outer mid-plane, where the curvature is bad in the toroidal angle with a bean-shape cross section, and it peaks around $\psi \sim 0.51\psi_w$. The mode amplitude peaks at the flux value where the poloidal harmonic number is $m = 74$, and the corresponding toroidal harmonic number is $n = 73$ with a frequency of $w_r = 1.54C_s/R_0$. The mode propagates in the ion diamagnetic direction having a growth rate of $\gamma = 0.51C_s/R_0$, and normalized perpendicular wave number $k_\perp\rho_i$=0.55.

## 3.2 ITG instability in QSTK

The linear ITG simulations for QSTK employ identical spatial resolutions and plasma profiles as those utilized in above analysis for W7-X. The simulation domain is restricted to $\psi_{outer} = 0.7\psi_w$ due to numerical issues in the QSTK EFIT data. The plasma profile parameters are carefully chosen to ensure the mode is localized within the computational domain, preventing boundary artifacts. The simulation time step used for the linear simulation is $\Delta t = 0.02R_0/C_s$ with $C_s/R_0 = 9.37 \times 10^4$ $\text{sec}^{-1}$. Furthermore, the major radius for the QSTK is $R_0 = 8.40$m, and the magnetic field on axis value is $B_0 = 1.01$T. In Fig. 4 (right) we show the mode structure of the electrostatic potential of
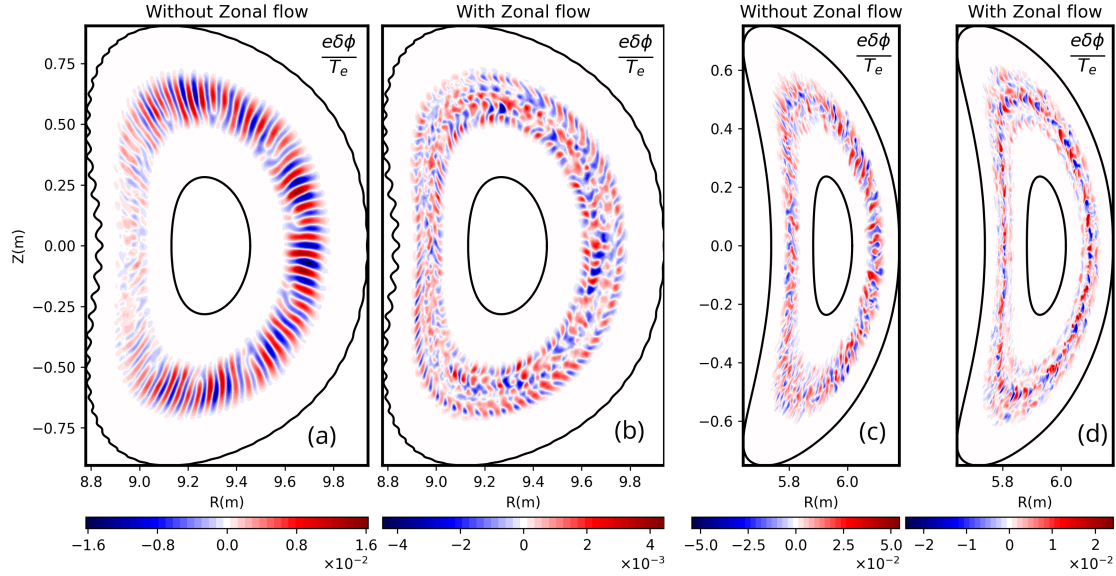
**Figure 5:** Contour plots of the electrostatic perturbed potential in the nonlinear phase for both machines with ion temperature gradient $a/L_{T_i} = 1.21$. (a) QSTK without ZFs, (b) QSTK with ZFs at $t = 55.0R_0/C_s$, (c) W7-X without ZFs, (d) W7-X with ZFs at $t = 45.0R_0/C_s$. The black curves indicate the inner and outer simulation boundaries.
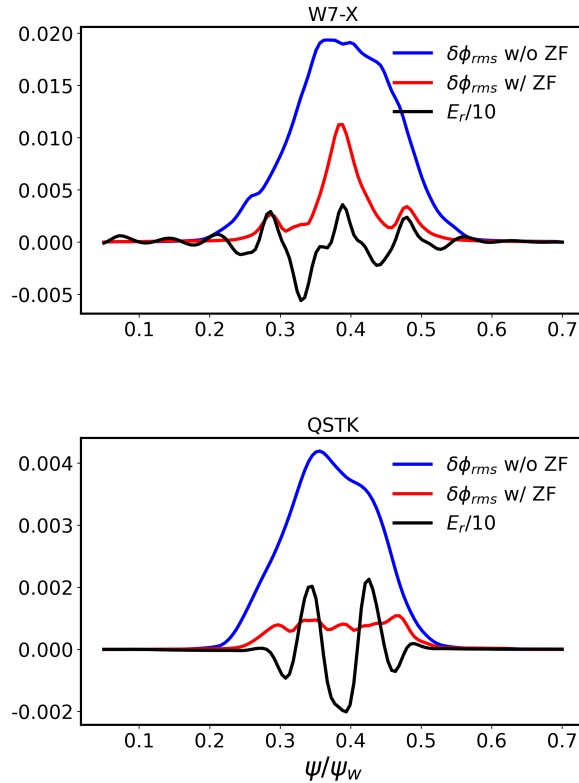


**Figure 6:** The flux surface variation of root-mean-squared electrostatic perturbed potential ($\delta\phi_{rms}$) with (blue line) and without (red line) zonal flow and the radial electric field ($E_r$) (black line) from the turbulence at the saturation stage of ITG turbulence at time $t = 55R_0/C_s$ for W7-X (top) and $t = 65R_0/C_s$ QSTK (bottom). The electrostatic potential is normalized with $T_e/e$, and the radial electric field resulting from the turbulence is normalized with $\sqrt{T_e/e}$. The ion temperature gradient, in this case, is $a/L_{T_i} = 1.21$.
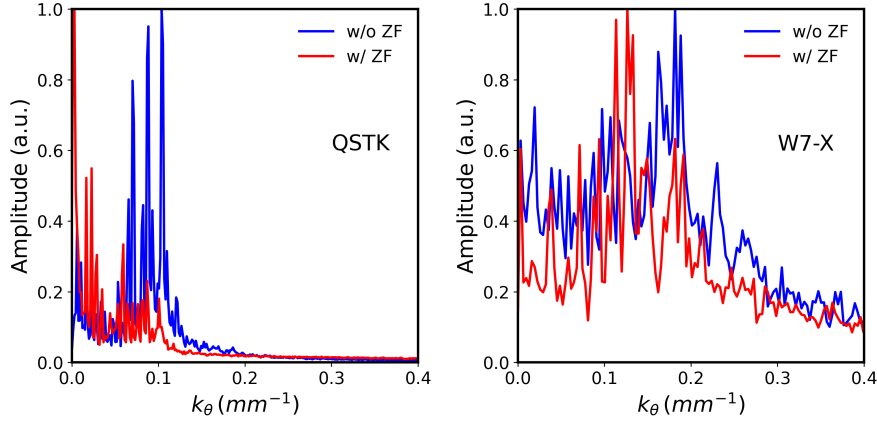
**Figure 7:** The poloidal wave number spectrum in QSTK (Left) and W7-X (Right) for the ion temperature gradient $a/L_{T_i} = 1.21$. The poloidal wave number decreases for both configurations in the presence of ZFs. For QSTK, the poloidal spectrum is plotted by taking the average over the saturation phase $t = [65.0, 72.5]R_0/C_s$ with and without ZFs. For W7-X, the same quantity is plotted by averaging over $t = [32.5, 40]R_0/C_s$ with and without ZFs.
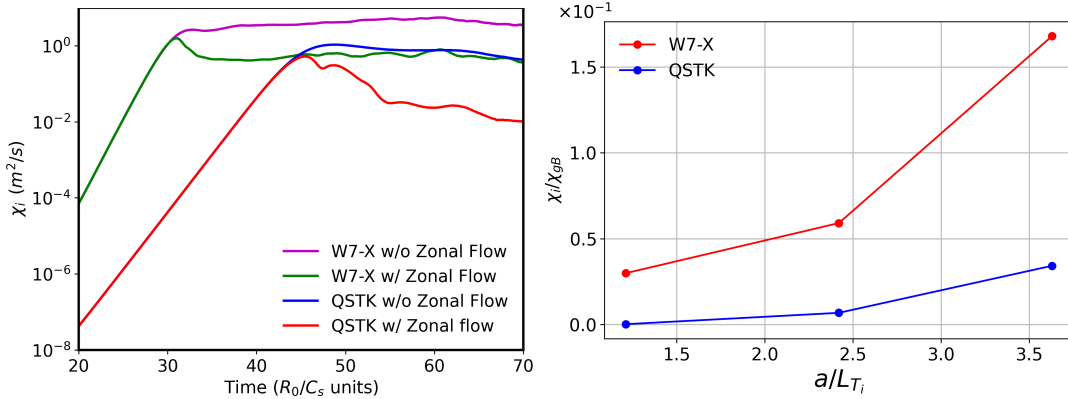


**Figure 8:** (Left) Comparison of ion heat conductivity ($\chi_i$) in QSTK and W7-X, with and without ZFs for the ion temperature gradient $a/L_{T_i} = 1.21$. (Right) In the presence of ZFs, the normalized ion heat diffusivity is plotted as a function of the ion temperature gradient. We see that the normalized ion heat diffusivity is lower in QSTK compared to the W7-X over the entire range of ion temperature gradient.

ITG on the $\zeta = 0$ poloidal plane for QSTK during the growing phase of the nonlinear simulation at $t = 37.5R_0/C_s$. The poloidal mode number and the toroidal mode numbers at the location where the eigenmode peaks ($\psi \sim 0.52\psi_w$) are $m = 59$ and $n = 63$, respectively, with a frequency $w_r = 2.64C_s/R_0$ propagating in the ion diamagnetic direction with growth rate $\gamma = 0.35\ C_s/R_0$ and normalized wave number $k_\perp\rho_i = 0.75$. In both QSTK and W7-X, the linear mode structures of ITG resemble the typical ballooning structure, localized on the outer midplane, and the widths of the linear modes (full width at half maximum) for both stellarators have almost similar values of 0.06 in units of $r/a$. At both sides of the radial simulation domain, fixed boundary conditions are applied for all fluctuating quantities, and all the out-of-boundary particles are brought back into the simulation domain through energy-conserving boundary conditions and by setting particle weight to be zero.

# 4    Nonlinear simulations of ITG in stellarators

In this section, we focus on the turbulence features for QSTK and W7-X using the same plasma profiles. Specifically, we study the effect of ZFs on the collisionless ITG saturation mechanism in

both W7-X and QSTK. The spatial resolutions and the marker particle numbers for these nonlinear simulations are the same as the linear cases; however, the time step for these simulations is $\Delta t = 0.01 R_0/C_s$. Fig. [5] represents the contour plots of the electrostatic potential in the nonlinear phase of ITG micro-turbulence in the absence (via numerical suppression) and presence of ZFs for the QSTK and W7-X stellarators. When zonal flows are artificially removed in the nonlinear phase, the linear mode structure spreads radially from the linear eigenmode due to nonlinear toroidal mode coupling Fig. 5[(a) and (c)]. Once we include ZFs in the simulation, the zonal shear breaks these eddies into fine structures Fig. 5[(b) and (d)]. To demonstrate the effect of ZFs on the electrostatic potential, we have calculated the root-mean-square value of $\delta\phi$ in the absence and presence of ZFs as the flux surface averaged radial electric field generated by turbulence at the nonlinear stage at $t = 55 R_0/C_s$, and for QSTK at $t = 65 R_0/C_s$, see Fig. (6). The difference in turbulence potential, shown by the red and blue lines, highlights the suppression of ITG turbulence by ZFs in both configurations. In W7-X, the suppression is $\sim 2.1$ times, while in QSTK, it is $\sim 5.9$ times, including ZFs, compared to the case without ZFs. This demonstrates the significant role of ZFs in reducing ITG-driven turbulent transport [23] in these two optimized stellarators.

To further evaluate the ZF effect, we have analyzed the poloidal spectrum of the time-averaged electrostatic potential during the nonlinear phase. Fig. 7 shows the time-averaged poloidal wave number spectrum for QSTK (left) and W7-X (right) in the presence and absence of ZFs. For QSTK, we consider the time average from $65.05 R_0/C_s$ to $72.5 R_0/C_s$ and for W7-X, from $47.5\ R_0/C_s$ to $52.5\ R_0/C_s$. The wave number spectra are broad due to the nonlinear mode coupling $k_\theta \in [0, 0.15]$ mm$^{-1}$ and $k_\theta \in [0, 0.4]$ mm$^{-1}$ for QSTK and W7-X, respectively, in the absence of ZFs. Interestingly, in Fig. 7, it is shown that the poloidal wave numbers move to a rather low value for QSTK, whereas high poloidal wave numbers still dominate for W7-X. We argue this is a result of the effects of CG optimization, which, by increasing the gradient of the binormal coordinate along magnetic field lines, stabilizes ITG modes with large poloidal wavenumbers relative to those with lower wavenumbers. The resulting low wavenumber modes are driven more weakly by toroidal curvature (through the drift factor $\mathbf{v}_d$ in the gyrokinetic equation) and are thus expected to have smaller relative growth rates.

Finally, to quantify the ZF effect on micro-turbulence, we computed the transport coefficients in these two configurations in the presence and absence of ZFs. Fig. 8 shows the time trace of ion heat conductivity, which is calculated in GTC as [33]

$$\chi_i = \frac{1}{\langle |\nabla\psi|^2\rangle n_i \frac{\partial T_i}{\partial \psi}} \left\langle \int d^3v \delta f \left( \frac{1}{2} m_i v^2 - \frac{3}{2} T_i \right) \mathbf{v_E} \cdot \nabla\psi \right\rangle$$

The result suggests that the turbulent transport increases exponentially in the linear phase and then saturates in the nonlinear phase, in which the effect of zonal flow on suppressing the heat transport is seen. The impact of ZFs on QSTK seems more pronounced when we compare it with W7-X, as shown in Table 1. We also performed a scan in ion temperature gradients ($a/L_{T_i} = [1.21, 2.42, 3.63]$), retaining ZFs, and calculated the normalized ion heat diffusivity in the right of Fig. 8. QSTK has lower ion heat diffusivity over the entire range of gradients, even above the apparent ITG threshold near $a/L_{T_i} = 1.2$. Further, the effect of ZFs on the reduction of $\chi_i$ decreases as the ion temperature gradient is increased, as shown in Table 1. The more modest (though still significant) suppression factors at higher gradients are expected once the CGs of both configurations are exceeded, as appears to be the case in light of the $a/L_T$ scan shown in Fig. 8, since both configurations produce finite heat fluxes at these gradients.

# 5 Conclusion and Discussion

In this work we have carried out the study of ITG-driven turbulence in the optimized stellarators W7-X and QSTK. The latter design resulted from a recent optimization study that targeted the critical gradient of the ITG mode [9]. We found a sensitivity of the turbulence saturation to the presence of zonal flows, which was especially strong in QSTK. Turbulence intensities, quantified by the ion heat flux, differed by a large factor ($\sim 48$) between the two stellarators at the lowest gradient, favoring the turbulence-optimized QSTK. Such a large relative factor at this gradient suggests threshold behavior in line with the targeting of a high linear critical gradient for ITG

**Table 1:** Comparison of the effect of ZF for the two stellarators. We compare the ion heat conductivity ($\chi_i$) in the nonlinear regime for the two cases listed below. The reduction is calculated by taking the ratio of the mean of $\chi_i$ in the nonlinear regime shown in Fig.( 8). We also compare the effect of temperature gradient on the reduction of $\chi_i$ in the presence of ZFs in the two machines.

| Case | $a/L_{T_i}$ | Reduction in $\chi_i$ |
|---|---|---|
| W7-X (w/o ZF) vs QSTK (w/o ZF) | 1.21 | $\sim 14.6$ |
| W7-X (w/ ZF) vs QSTK(w/ ZF) | 1.21 | $\sim 48.1$ |
| W7-X (w/ ZF) vs QSTK(w/ ZF) | 2.42 | $\sim 8.6$ |
| W7-X (w/ ZF) vs QSTK(w/ ZF) | 3.63 | $\sim 4.9$ |

modes in QSTK. At higher temperature gradients, apparently above this threshold, QSTK continues to enjoy lower nonlinear heat fluxes in comparison to W7-X, perhaps in part because of reduced linear growth rates for ITG modes. We thus expect CG optimization to continue to be useful in guiding stellarator design for reduced ion transport, whether as a result of improved thresholds at low gradients, lower growth rates at high gradients, or through some interplay of the two effects.

## Acknowledgments

## References

[1] Lyman Spitzer Jr. The stellarator concept. *The Physics of Fluids*, 1(4):253–264, 1958.

[2] Javier H. Nicolau, Gyungjin Choi, Jingyuan Fu, Pengfei Liu, Xishuo Wei, and Zhihong Lin. Global gyrokinetic simulation with kinetic electron for collisionless damping of zonal flow in stellarators. *Nuclear Fusion*, 61(12):126041, nov 2021.

[3] Alexey Mishchenko, Per Helander, and Axel Könies. Collisionless dynamics of zonal flows in stellarator geometry. *Physics of Plasmas*, 15(7):072309, 2008.

[4] C. D. Beidler, H. M. Smith, A. Alonso, et al. Demonstration of reduced neoclassical energy transport in Wendelstein 7-X. *Nature*, 596:221–226, 2021.

[5] A. Dinklage, C. D. Beidler, P. Helander, et al. Magnetic configuration effects on the Wendelstein 7-X stellarator. *Nature Physics*, 14:855–860, 2018.

[6] D. Carralero, T. Estrada, E. Maragkoudakis, T. Windisch, J.A. Alonso, M. Beurskens, S. Bozhenkov, I. Calvo, H. Damm, O. Ford, G. Fuchert, J.M. García-Regaña, N. Pablant, E. Sánchez, E. Pasch, J.L. Velasco, and the Wendelstein 7-X team. An experimental characterization of core turbulence regimes in wendelstein 7-x. *Nuclear Fusion*, 61(9):096015, aug 2021.

[7] M.N.A. Beurskens, S.A. Bozhenkov, O. Ford, P. Xanthopoulos, A. Zocco, Y. Turkin, A. Alonso, C. Beidler, I. Calvo, D. Carralero, T. Estrada, G. Fuchert, O. Grulke, M. Hirsch, K. Ida, M. Jakubowski, C. Killer, M. Krychowiak, S. Kwak, S. Lazerson, A. Langenberg, R. Lunsford, N. Pablant, E. Pasch, A. Pavone, F. Reimold, Th. Romba, A. von Stechow, H.M. Smith,

T. Windisch, M. Yoshinuma, D. Zhang, R.C. Wolf, and the W7-X Team. Ion temperature clamping in wendelstein 7-x electron cyclotron heated plasmas. *Nuclear Fusion*, 61(11):116072, oct 2021.

[8] E. M. Edlund, M. Porkolab, Z. Huang, O. Grulke, L.-G. Böttger, C. von Sehren, and A. von Stechow. Overview of the Wendelstein 7-X phase contrast imaging diagnostic. *Review of Scientific Instruments*, 89(10):10E105, 08 2018.

[9] G. T. Roberg-Clark, G. G. Plunk, P. Xanthopoulos, C. Nührenberg, S. A. Henneberg, and H. M. Smith. Critical gradient turbulence optimization toward a compact stellarator reactor concept. *Phys. Rev. Res.*, 5:L032030, Sep 2023.

[10] L. Podavini, A. Zocco, J. M. García-Regaña, M. Barnes, F. I. Parra, A. Mishchenko, and P. Helander. Ion temperature and density gradient driven instabilities and turbulence in wendelstein 7-x close to the stability threshold. 90(4):905900414, Aug 2024.

[11] Animesh Kuley and V. K. Tripathi. Stabilization of ion temperature gradient driven modes by lower hybrid wave in a tokamak. *Physics of Plasmas*, 16(3):032504, Mar 2009.

[12] Animesh Kuley, C. S. Liu, and V. K. Tripathi. Lower hybrid destabilization of trapped electron modes in tokamak and its consequences for anomalous diffusion. *Physics of Plasmas*, 17(7):072506, Jul 2010.

[13] R. Kleiber, M. Borchardt, R. Hatzky, A. Könies, H. Leyh, A. Mishchenko, J. Riemann, C. Slaby, J.M. García-Regaña, E. Sánchez, and M. Cole. Euterpe: A global gyrokinetic code for stellarator geometry. *Computer Physics Communications*, 295:109013, 2024.

[14] J Riemann, R Kleiber, and M Borchardt. Effects of radial electric fields on linear itg instabilities in w7-x and lhd. *Plasma Physics and Controlled Fusion*, 58(7):074001, may 2016.

[15] H. Thienpondt, J.M. García-Regaña, I. Calvo, G. Acton, and M. Barnes. Influence of the density gradient on turbulent heat transport at ion-scales: an inter-machine study with the gyrokinetic code stella. *Nuclear Fusion*, 65(1):016062, dec 2024.

[16] Motoki Nakata, Masanori Nunami, Hideo Sugama, and Tomo-Hiko Watanabe. Isotope effects on trapped-electron-mode driven turbulence and zonal flows in helical and tokamak plasmas. *Phys. Rev. Lett.*, 118:165002, Apr 2017.

[17] H. E. Mynick, N. Pomphrey, and P. Xanthopoulos. Reducing turbulent transport in toroidal configurations via shaping. *Physics of Plasmas*, 18(5):056101, 2011.

[18] A. Bañón Navarro, A. Di Siena, J.L. Velasco, F. Wilms, G. Merlo, T. Windisch, L.L. LoDestro, J.B. Parker, and F. Jenko. First-principles based plasma profile predictions for optimized stellarators. *Nuclear Fusion*, 63(5):054003, mar 2023.

[19] A. Bañón Navarro, G. T. Roberg-Clark, G. G. Plunk, D. Fernando, A. Di Siena, F. Wilms, and F. Jenko. Assessing core ion thermal confinement in critical-gradient-optimized stellarators. *Physics of Plasmas*, 31(6):062508, 06 2024.

[20] Seikichi Matsuoka, Yasuhiro Idomura, and Shinsuke Satake. Neoclassical transport benchmark of global full-f gyrokinetic simulation in stellarator configurations. *Physics of Plasmas*, 25(2):022510, 02 2018.

[21] M. D. J. Cole, T. Moritaka, R. Hager, J. Dominski, S. Ku, and C. S. Chang. Nonlinear global gyrokinetic delta-f turbulence simulations in a quasi-axisymmetric stellarator. *Physics of Plasmas*, 27(4):044501, 04 2020.

[22] A Bañón Navarro, G Merlo, G G Plunk, P Xanthopoulos, A von Stechow, A Di Siena, M Maurer, F Hindenlang, F Wilms, and F Jenko. Global gyrokinetic simulations of itg turbulence in the magnetic configuration space of the wendelstein 7-x stellarator. *Plasma Physics and Controlled Fusion*, 62(10):105005, aug 2020.

[23] Tajinder Singh, Javier H. Nicolau, Zhihong Lin, Sarveshwar Sharma, Abhijit Sen, and Animesh Kuley. Global gyrokinetic simulations of electrostatic microturbulent transport using kinetic electrons in lhd stellarator. *Nuclear Fusion*, 62(12):126006, oct 2022.

[24] Tajinder Singh, Javier H. Nicolau, Federico Nespoli, Gen Motojima, Zhihong Lin, Abhijit Sen, Sarveshwar Sharma, and Animesh Kuley. Global gyrokinetic simulations of electrostatic microturbulent transport in lhd stellarator with boron impurity. *Nuclear Fusion*, 64(1):016007, nov 2024.

[25] A.J. Coelho, J. Loizu, P. Ricci, and Z. Tecchiolli. Global fluid simulation of plasma turbulence in stellarators with the gbs code. *Nuclear Fusion*, 64(7):076057, jun 2024.

[26] B Shanahan, B Dudson, and P Hill. Fluid simulations of plasma filaments in stellarator geometries with bsting. *Plasma Physics and Controlled Fusion*, 61(2):025007, dec 2018.

[27] B. Shanahan, D. Bold, and B. Dudson. Global fluid turbulence simulations in the scrape-off layer of a stellarator island divertor. *Journal of Plasma Physics*, 90(2):905900216, 2024.

[28] H. Y. Wang, I. Holod, Z. Lin, J. Bao, J. Y. Fu, P. F. Liu, J. H. Nicolau, D. Spong, and Y. Xiao. Global gyrokinetic particle simulations of microturbulence in W7-X and LHD stellarators. *Physics of Plasmas*, 27(8):082305, 08 2020.

[29] J. Y. Fu, J. H. Nicolau, P. F. Liu, X. S. Wei, Y. Xiao, and Z. Lin. Global gyrokinetic simulation of neoclassical ambipolar electric field and its effects on microturbulence in W7-X stellarator. *Physics of Plasmas*, 28(6):062309, 06 2021.

[30] Y Q Qin, Y C Chen, G Y Sun, J Nicolau, and Z Lin. Effects of hydrogen isotope species on itg microturbulence in lhd. *Plasma Physics and Controlled Fusion*, 66(8):085004, jun 2024.

[31] Z. Lin, T. S. Hahm, W. W. Lee, W. M. Tang, and R. B. White. Turbulent transport reduction by zonal flows: Massively parallel simulations. *Science*, 281(5384):1835–1837, 1998.

[32] Yong Xiao and Zhihong Lin. Turbulent transport of trapped-electron modes in collisionless plasmas. *Phys. Rev. Lett.*, 103:085004, Aug 2009.

[33] Tajinder Singh, Deepti Sharma, Tanmay Macwan, Sarveshwar Sharma, Joydeep Ghosh, Abhijit Sen, Zhihong Lin, and Animesh Kuley. Gyrokinetic simulations of electrostatic microturbulence in aditya-u tokamak. *Nuclear Fusion*, 63(5):056008, mar 2023.

[34] Tajinder Singh, Kajal Shah, Deepti Sharma, Joydeep Ghosh, Kumarpalsinh A. Jadeja, Rakesh L. Tanna, M.B. Chowdhuri, Zhihong Lin, Abhijit Sen, Sarveshwar Sharma, and Animesh Kuley. Gyrokinetic simulations of electrostatic microturbulence in aditya-u tokamak with argon impurity. *Nuclear Fusion*, 64(8):086038, jun 2024.

[35] Zhixuan Wang, Zhihong Lin, Ihor Holod, W. W. Heidbrink, Benjamin Tobias, Michael Van Zeeland, and M. E. Austin. Radial localization of toroidicity-induced alfvén eigenmodes. *Phys. Rev. Lett.*, 111:145003, Oct 2013.

[36] Wenlu Zhang, Zhihong Lin, and Liu Chen. Transport of energetic particles by microturbulence in magnetized plasmas. *Phys. Rev. Lett.*, 101:095001, Aug 2008.

[37] G. Brochard, C. Liu, X. Wei, W. Heidbrink, Z. Lin, N. Gorelenkov, C. Chrystal, X. Du, J. Bao, A. R. Polevoi, M. Schneider, S. H. Kim, S. D. Pinches, P. Liu, J. H. Nicolau, and H. Lütjens. Saturation of fishbone instability by self-generated zonal flows in tokamak plasmas. *Phys. Rev. Lett.*, 132:075101, Feb 2024.

[38] Animesh Kuley, Z. X. Wang, Z. Lin, and F. Wessel. Verification of particle simulation of radio frequency waves in fusion plasmas. *Physics of Plasmas*, 20(10):102515, 10 2013.

[39] A. Kuley, Z. Lin, J. Bao, X. S. Wei, Y. Xiao, W. Zhang, G. Y. Sun, and N. J. Fisch. Verification of nonlinear particle simulation of radio frequency waves in tokamak. *Physics of Plasmas*, 22(10):102515, 10 2015.

[40] J. Bao, Z. Lin, A. Kuley, and Z.X. Wang. Electromagnetic particle simulation of the effect of toroidicity on linear mode conversion and absorption of lower hybrid waves. *Nuclear Fusion*, 56(6):066007, may 2016.

[41] Z. Lin, T. S. Hahm, W. W. Lee, W. M. Tang, and P. H. Diamond. Effects of collisional zonal flow damping on turbulent transport. *Phys. Rev. Lett.*, 83:3645–3648, Nov 1999.

[42] S. P. Hirshman and J. C. Whitson. Steepest-descent moment method for three-dimensional magnetohydrodynamic equilibria. *Physics of Fluids*, 26(12):3553–3568, Dec 1983.

[43] S. E. Parker and W. W. Lee. A fully nonlinear characteristic method for gyrokinetic simulation. *Physics of Fluids B: Plasma Physics*, 5(1):77–86, 01 1993.